ChemComm

COMMUNICATION

Direct growth of flexible LiMn$_2$O$_4$/CNT lithium-ion cathodes†

Xilai Jia,‡[ab] Chunzhu Yan,‡[ac] Zheng Chen,[a] Ranran Wang,[a] Qiang Zhang,[b] Lin Guo,*[c] Fei Wei*[b] and Yunfeng Lu*[a]

Flexible, binder-free LiMn$_2$O$_4$/CNT nanocomposites with good reversible capability and cycling stability were fabricated by *in-situ* hydrothermal growth for flexible lithium battery applications.

Flexible lithium-ion batteries hold great promise for rollup displays, smart electronics, wearable devices and other applications.[1] Their large-scale use, however, is limited by our capability to fabricate flexible lithium-ion electrodes and device packaging, and by other technical difficulties. Recently, several flexible anodes have been reported, such as those based on composites of carbon nanotubes (CNTs) (or graphene) and active anode materials[2] and composites of graphite and fibrillated cellulose.[3] However, the fabrication of flexible cathodes has been more difficult. One reason is that commonly used cathode materials, such as LiCoO$_2$, LiMn$_2$O$_4$ and LiFePO$_4$, are generally synthesized in high-temperature environments,[4] while most flexible substrates or materials used to make flexible substrates are unstable under such processing conditions. One possible strategy to circumvent this difficulty is to fabricate cathodes by mixing particulate cathode materials with polymer binders and conductive agents and then coating the mixtures on flexible substrates.

Here, we report a direct-growth method to make high-performance flexible cathodes. Using LiMn$_2$O$_4$ based flexible cathodes as an example, we started with flexible CNT networks that were mildly pre-oxidized. Spontaneous redox reactions between the CNTs and KMnO$_4$ generated layers of MnO$_2$ wrapped around the CNTs. Subsequent hydrothermal treatment in the presence of LiOH converted the MnO$_2$/CNT composites into LiMn$_2$O$_4$/CNT composites. Vacuum filtration of the composites created free-standing cathodes that are binder-free and flexible.

[a] Department of Chemical and Biomolecular Engineering, University of California, Los Angeles, CA 90095, USA.
E-mail: luucla@ucla.edu; Fax: +1 310-206-410;
Tel: +1 310-794-7238
[b] Beijing Key Laboratory of Green Chemical Reaction Engineering and Technology, Department of Chemical Engineering, Tsinghua University, Beijing 100084, P. R. China.
E-mail: wf-dce@tsinghua.edu.cn
[c] School of Chemistry and Environment, Beihang University, Beijing 100191, P. R. China. E-mail: guolin@buaa.edu.cn
† Electronic supplementary information (ESI) available: Experimental details, BET, TGA, SEM. See DOI: 10.1039/c1cc13536h
‡ Both authors contributed equally to this work.
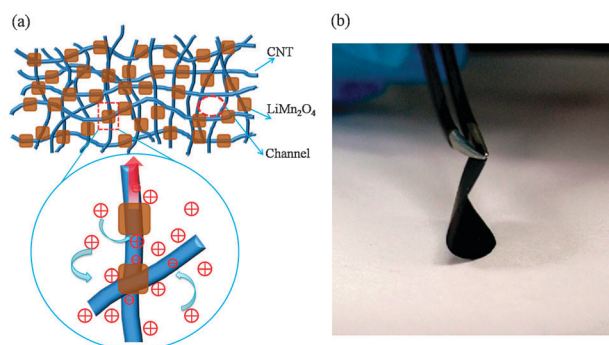
Fig. 1 (a) Schematic illustration of the structure of the flexible LiMn$_2$O$_4$/CNT nanocomposite cathodes and (b) a photograph showing an as-synthesized flexible electrode.

Fig. 1a shows a schematic of the structure of such flexible electrodes. Compared with electrodes made by the traditional coating approach, our flexible cathodes exhibit several unique features. First, these cathodes consist of networks of CNTs and LiMn$_2$O$_4$ nanocrystals. The CNT networks provide a flexible, conductive and porous scaffold, facilitating ion and electron transport; while the small size of the LiMn$_2$O$_4$ nanocrystals shortens lithium-ion diffusion length within the crystals. Furthermore, as-formed LiMn$_2$O$_4$ nanocrystals are threaded through the CNTs, forming intimate and robust interfaces between the nanocrystals and the conductive CNT network. All these features are essential to ensuring good electrode performance.

Fig. 1b shows a photograph of a representative flexible electrode with a thickness of around 30–40 μm. The structure of these composite electrodes was investigated using X-ray diffraction (XRD) and electron microscopic techniques. Fig. 2 shows XRD patterns of the LiMn$_2$O$_4$/CNT composite, the MnO$_2$/CNT composite and the mildly oxidized CNTs. The CNTs show typical graphite (002) and (100) reflections at two theta of 26.2° and 43.6°, respectively.[5] The MnO$_2$/CNT composite exhibits a broad diffraction hump from 20° to 25°, suggesting the presence of amorphous domains. Weak diffraction peaks at 25.5°, 37.3°, and 67.2° are also observed, suggesting that MnO$_2$ with a hydrous birnessite structure (JCPDS: 42-1317) is also present.[6] Note that the characteristic CNT diffraction peak at 26.2° is not visible, indicating an extensive oxidation reaction between the CNTs and KMnO$_4$, which is consistent with the formation of a thick MnO$_2$ layer
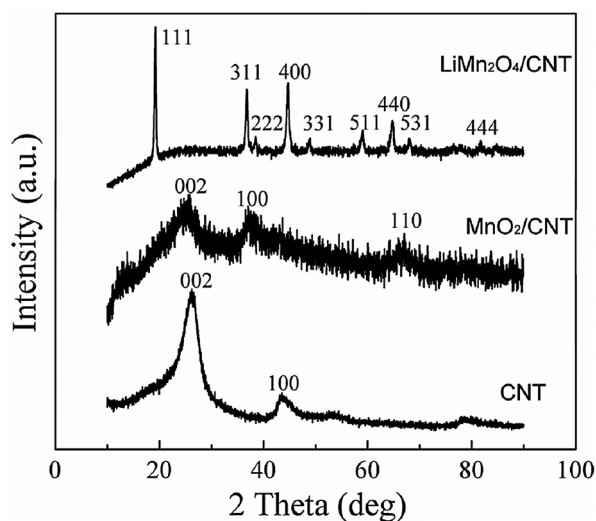
Fig. 2 XRD patterns of LiMn₂O₄/CNT composite, MnO₂/CNT composite, and CNTs used to synthesize these composites.
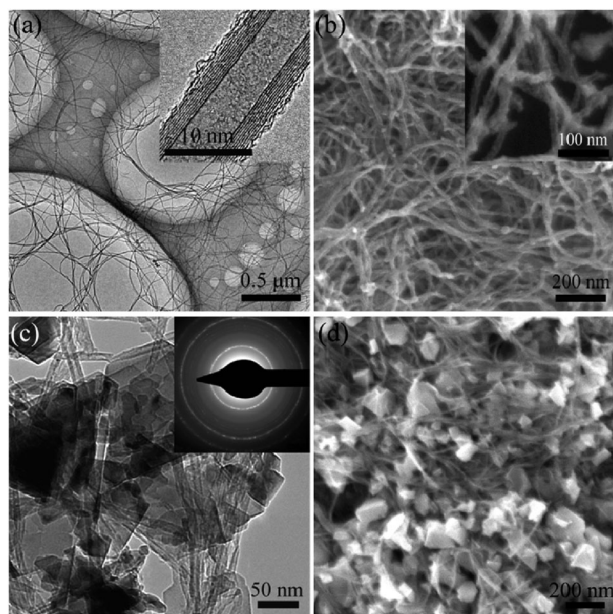
Fig. 3 (a) TEM image of the CNTs used, (b) SEM image of the MnO₂/CNT composite, (c) TEM image of the LiMn₂O₄/CNT nano-composite, and (d) SEM image of the LiMn₂O₄/CNT composite.

outside the CNT walls (see Fig. 3b). By comparison, the LiMn$_2$O$_4$/CNT composite exhibits intense diffraction peaks of spinel LiMn$_2$O$_4$ (space group $Fd3m$, JCPDS card No. 35-0782). The absence of birnessite MnO$_2$ diffractions suggests a successful transformation of MnO$_2$ to LiMn$_2$O$_4$. Similar to the MnO$_2$/CNT composite, no diffraction peak corresponding to CNTs was observed in the XRD pattern of LiMn$_2$O$_4$/CNT composites (Fig. S1, ESI†). It is worth mentioning that direct reaction of γ-MnO$_2$ with LiOH at the same hydrothermal conditions has failed to afford LiMn$_2$O$_4$. Much higher synthesis temperatures (200–280 °C) are often required[7] to convert γ-MnO$_2$ into LiMn$_2$O$_4$, which are much higher than that used in this work (180 °C).

Fig. 3a shows transmission electron microscopic (TEM) images of the CNTs. These CNTs are of a uniform diameter of around 11 nm (TEM image, inset to Fig. 1a) and up to 100 μm in length.[8] Such high aspect ratio CNTs form a highly flexible scaffold for composite electrodes. Upon reacting the CNTs with KMnO$_4$, uniform MnO$_2$ was formed on the CNTs. As shown by the scanning electron microscopic (SEM) image in Fig. 3b, these MnO$_2$/CNT composite tubes exhibit a uniform diameter of around 20 nm, which is twice that of the original CNTs, indicating extensive growth of MnO$_2$. Direct measurement of the weight of CNTs (0.2 g) and as-grown MnO$_2$/CNTs (1.1 g) further confirmed that ∼45 wt% of the CNTs was involved in the redox reaction based on stoichiometry (Fig. S2, ESI†). In addition, the composite nanotubes further form an interpenetrating fibrous network.

After the hydrothermal reaction, the uniform MnO$_2$ coatings were converted to LiMn$_2$O$_4$ nanocrystals, which are threaded with CNT networks (see SEM image in Fig. 3d). The LiMn$_2$O$_4$ nanocrystal size is mainly distributed between 50 and 100 nm (Fig. S3, ESI†). Since the LiMn$_2$O$_4$ nanocrystals were directly grown from the MnO$_2$ coatings on the CNTs, they are strongly bound to the CNTs, ensuring intimate contact for better charge transport. Fig. 3c shows a TEM image of the LiMn$_2$O$_4$ composite, confirming the close contacts between the CNTs and the nanocrystals. Selected area electron diffraction (SAED, inset of Fig. 3c) reveals the polycrystalline nature of the LiMn$_2$O$_4$. CNT diameter in the final nanocomposite averaged 8.5 nm, which is consistent with the reaction stoichiometry (Fig. S2, ESI†). In comparison, directly mixing LiMn$_2$O$_4$ nanoparticles with CNTs in the same mass ratio did not result in a continuous, flexible film due to the weak interaction between the particles and CNTs.

Their unique interpenetrating structure provides the LiMn$_2$O$_4$/CNT composites with interconnected, three-dimensional porous channels. Fig. S4 (ESI†) shows representative nitrogen absorption isotherms of a LiMn$_2$O$_4$/CNT nanocomposite, indicating a surface area of 59.7 m^2 g^{-1} and a broad pore size distribution centered at 40 nm. Thermogravimetric analysis indicates that the composite contains 89 wt-% of LiMn$_2$O$_4$.

The electrical energy storage capability of the composite electrodes was first examined using cyclic voltammetry (CV). Fig. 4a shows the CV profile of a LiMn$_2$O$_4$/CNT electrode assembled in a coin-type half cell using lithium as both counter and reference electrodes. At a scan rate of 0.2 mV s^{-1}, two pairs of well defined redox peaks are observed at around 4.06/3.95 V and 4.2/4.1 V, respectively. These features suggest that Li$^+$ can be extracted from and inserted into the electrode reversibly, which is consistent with that of typical spinel LiMn$_2$O$_4$, where tetrahedral sites are involved in the charge/discharge process.[9]

Fig. 4b shows constant current charge/discharge profiles of the LiMn$_2$O$_4$/CNT electrode between the cutoff voltages of 3.2 and 4.3 V at a current density of 22 mA g^{-1}. The charge/discharge curves present two distinguished plateaus, respectively, which reflects a two-stage Li$^+$ insertion/extraction behavior and is consistent with both the CV curves obtained and other reports.[9] The initial charge and discharge capacities
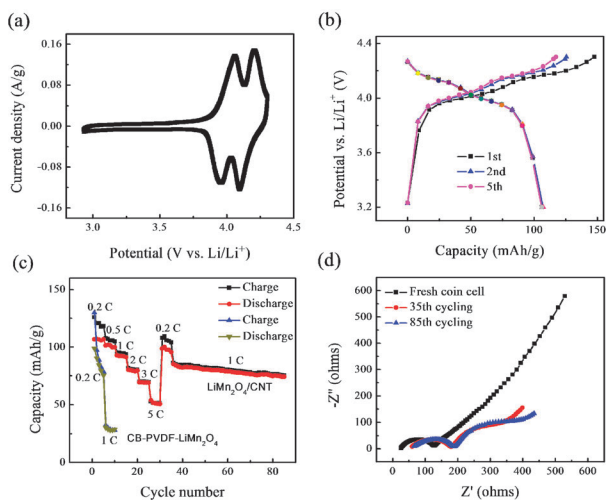
Fig. 4 (a) CV curves of the nanocomposite electrodes between potential limits of 2.9 and 4.3 V at a scanning rate of 0.2 mV s^{-1}, (b) charge/discharge curves at a current density of 22 mA g^{-1}, (c) comparison of cyclic performance of the flexible LiMn$_2$O$_4$/CNT electrodes and the traditional LiMn$_2$O$_4$ composite electrode fabricated using polymer binder (PVDF) and carbon black (CB), (d) electrochemical impedance spectra of the flexible LiMn$_2$O$_4$/CNT electrode before and after cycling.

of the hybrid cathode were 126 and 109 mA h g^{-1}, respectively, corresponding to a coulombic efficiency of 86.5%. The low coulombic efficiency of the first cycle is due to the formation of a solid–electrolyte-interface (SEI) and is commonly observed for a variety of electrode materials. The charge/discharge efficiency approached 100% after a few cycles and remained stable in the following cycling, indicating good reversibility. Although somewhat higher capacities of ∼120 mA h g^{-1} have been reported for LiMn$_2$O$_4$ prepared using a solid-state synthesis, our electrodes avoid the use of polymer binder (∼10% in total weight), and hence provide higher overall storage capability.

Fig. 4c shows the flexible LiMn$_2$O$_4$ electrode's capacity dependence on the charge/discharge rate and cycling number. The rate capability of this binder-free cathode is impressive. For example, at a relatively high current density of 550 mA g^{-1}, the composite material still delivered a discharge capacity of 50 mA h g^{-1}. As shown in Fig. 4c, upon returning back to a rate of 0.2 C after 30 cycles at different rates, the composite cathode can still deliver the same capacity of 102 mA h g^{-1}. Even after 50 subsequent cycles at 1.0 C, a capacity of 80 mA h g^{-1} can still be retained, suggesting good cycling stability. The slow capacity degradation is a common behavior that results from the intrinsic cycling instability of LiMn$_2$O$_4$.[9] Overall, the performance of the flexible LiMn$_2$O$_4$ electrodes is much better than the LiMn$_2$O$_4$ nanoparticle-based composite electrode fabricated using polymer binder and carbon black.

Electrochemical impedance spectroscopy (EIS) was conducted to further investigate the interface characteristics between LiMn$_2$O$_4$ and CNTs (Fig. 4d). The fresh electrode exhibits a single semicircle at high frequency, which is attributed to a combination of resistance, capacitance, and constant phase

elements on the electrode.[9] After 35 cycles, the EIS plot shows increased internal resistance and another semicircle at lower frequency, which is ascribed to the formation of a SEI layer and to surface reactions. The impedance behavior shows similar features after 85 cycles, indicating an invariant interface between LiMn$_2$O$_4$ and CNTs, which results in stable electrode processes and good cycling performance. To further confirm this, we opened the cycled cell and did SEM observation for the LiMn$_2$O$_4$/CNT electrode. As shown in Fig. S6 (ESI†), the electrode can still preserve a CNT network structure with LiMn$_2$O$_4$ nanoparticles anchored inside, suggesting the electrode structure integrity after long-term cycling.

In summary, we have demonstrated an efficient *in-situ* hydrothermal process to synthesize a class of flexible, binder-free hybrid cathode materials. These materials show high capacity and stable cycling performance, and thus have a great potential for flexible lithium ion batteries. This simple method may be extended to synthesize other flexible hybrid electrodes for energy storage devices.

Notes and references

1 (*a*) V. L. Pushparaj, M. M. Shaijumon, A. Kumar, S. Murugesan, L. Ci, R. Vajtai, R. J. Linhardt, O. Nalamasu and P. M. Ajayan, *Proc. Natl. Acad. Sci. U. S. A.*, 2007, **104**, 13574; (*b*) C. M. Ban, Z. C. Wu, D. T. Gillaspie, L. Chen, Y. F. Yan, J. L. Blackburn and A. C. Dillon, *Adv. Mater.*, 2010, **22**, E145; (*c*) T. Suga, H. Konishi and H. Nishide, *Chem. Commun.*, 2007, 1730.
2 (*a*) S. Y. Chew, S. H. Ng, J. Wang, P. Novák, F. Krumeich, S. L. Chou, J. Chen and H. K. Liu, *Carbon*, 2009, **47**, 2976; (*b*) D. Wang, R. Kou, D. Choi, Z. Yang, Z. Nie, J. Li, L. V. Saraf, D. Hu, J. Zhang, G. L. Graff, J. Liu, M. A. Pope and I. A. Aksay, *ACS Nano*, 2010, **4**, 1587; (*c*) H. Gwon, H.-S. Kim, K. U. Lee, D.-H. Seo, Y. C. Park, Y.-S. Lee, B. T. Ahn and K. Kang, *Energy Environ. Sci.*, 2011, **4**, 1277.
3 L. Jabbour, C. Gerbaldi, D. Chaussy, E. Zeno, S. Bodoardo and D. Beneventi, *J. Mater. Chem.*, 2010, **20**, 7344.
4 (*a*) M. S. Whittingham, *Chem. Rev.*, 2004, **104**, 4271; (*b*) Y. G. Wang, W. R. Wang, E. Hosono, K. X. Wang and H. S. Zhou, *Angew. Chem., Int. Ed.*, 2008, **47**, 7461.
5 Z. Q. Li, C. J. Lu, Z. P. Xia, Y. Zhou and Z. Luo, *Carbon*, 2007, **45**, 1686.
6 (*a*) X. B. Jin, W. Z. Zhou, S. W. Zhang and Z. C. George, *Small*, 2007, **3**, 1513; (*b*) X. L. Xiao, J. Lu and Y. D. Li, *Nano Res.*, 2010, **3**, 733; (*c*) Y. T. Peng, Z. Chen, J. Wen, Q. F. Xiao, D. Weng, S. Y. He, H. B. Geng and Y. F. Lu, *Nano Res.*, 2011, **4**, 216.
7 (*a*) C. H. Jiang, S. X. Dou, H. K. Liu, M. Ichihara and H. S. Zhou, *J. Power Sources*, 2007, **172**, 410; (*b*) H. M. Wu, J. P. Tu, Y. F. Yuan, X. T. Chen, J. Y. Xiang, X. B. Zhao and G. S. Cao, *J. Power Sources*, 2006, **161**, 1260.
8 Q. Zhang, M. Q. Zhao, J. Q. Huang, J. Q. Nie and F. Wei, *Carbon*, 2010, **48**, 1196.
9 (*a*) M. Okubo, Y. Mizuno, H. Yamada, J. Kim, E. Hosono, H. S. Zhou, T. Kudo and I. Honma, *ACS Nano*, 2010, **4**, 741; (*b*) H. J. Yue, X. K. Huang, D. P. Lv and Y. Yang, *Electrochim. Acta*, 2009, **54**, 5363; (*c*) X. M. Liu, Z. D. Huang, S. Oh, P. C. Ma, P. C. H. Chan, G. K. Vedam, K. Kang and J. K. Kim, *J. Power Sources*, 2010, **195**, 4290.